

Less effective hydrodynamic escape of H₂-H₂O atmospheres on terrestrial planets orbiting pre-main sequence M dwarfs

TATSUYA YOSHIDA,¹ NAOKI TERADA,¹ MASAHIRO IKOMA,² AND KIYOSHI KURAMOTO³

¹*Faculty of Science, Tohoku University, Sendai, Miyagi 980-8578, Japan*

²*Division of Science, National Astronomical Observatory of Japan, Mitaka, Tokyo 181-8588, Japan*

³*Faculty of Science, Hokkaido University, Sapporo, Hokkaido 060-0810, Japan*

ABSTRACT

Terrestrial planets currently in the habitable zones around M dwarfs likely experienced a long-term runaway greenhouse condition because of a slow decline in host-stellar luminosity in its pre-main sequence phase. Accordingly, they might have lost significant portions of their atmospheres including water vapor at high concentration by hydrodynamic escape induced by the strong stellar XUV irradiation. However, the atmospheric escape rates remain highly uncertain due partly to a lack of understanding of the effect of radiative cooling in the escape outflows. Here we carry out 1-D hydrodynamic escape simulations for an H₂-H₂O atmosphere on a planet with mass of $1M_{\oplus}$ considering radiative and chemical processes to estimate the atmospheric escape rate and follow the atmospheric evolution during the early runaway greenhouse phase. We find that the atmospheric escape rate decreases with the basal H₂O/H₂ ratio due to the energy loss by the radiative cooling of H₂O and chemical products such as OH and H₃⁺: the escape rate of H₂ becomes one order of magnitude smaller when the basal H₂O/H₂ = 0.1 than that of the pure hydrogen atmosphere. The timescale for H₂ escape exceeds the duration of the early runaway greenhouse phase, depending on the initial atmospheric amount and composition, indicating that H₂ and H₂O could be left behind after the end of the runaway greenhouse phase. Our results suggest that temperate and reducing environments with oceans could be formed on some terrestrial planets around M dwarfs.

Keywords: Exoplanet evolution (491) — Exoplanet atmospheres (487) — Upper atmosphere (1748)

1. INTRODUCTION

Planets around M dwarfs are thought to have difficulty in becoming habitable. During the pre-main sequence phase, M dwarfs are theoretically predicted to be 1 or even 2 orders of magnitude more luminous than when they reach the main sequence, and take up to 1 Gyr to settle onto the main sequence (Baraffe et al., 1998). Thus, planets currently in the habitable zones in the main sequence phase are likely to have been in runaway greenhouse conditions, provided they had sufficient surface water (e.g., Luger and Barnes, 2015). Moreover, XUV irradiation in the habitable zones around M dwarfs is estimated to be much stronger than that around Sun-like stars (e.g., Wheatley et al. 2017). Accordingly, terrestrial planets around M dwarfs likely lose significant portions of their atmospheres including water vapor at high concentration by hydrodynamic escape during the early runaway greenhouse phase. Previous studies demonstrated that such planets lose water with the amount equivalent to that in several Earth's oceans by hydrodynamic escape and some O₂ accumulates as residue depending on the XUV flux and planetary mass (e.g., Luger and Barnes, 2015). Such massive water loss and accumulation of oxygen have negative effects on the origin of life in that liquid water is likely essential for life and highly oxidized environments are unsuitable for the formation of important prebiotic organic molecules (e.g., Schlesinger and Miller, 1983).

Previous studies on atmospheric hydrodynamic escape for terrestrial planets orbiting M dwarfs considered mainly pure H₂O atmospheres (Luger and Barnes, 2015; Tian, 2015; Tian and Ida, 2015; Bolmont et al. 2017; Bourrier et al. 2017; Johnstone, 2020) or nebula-captured H₂-dominated atmospheres (Luger et al., 2015; Owen and Mohanty, 2016; Hori and Ogihara, 2020). On the other hand, planet formation theories suggest that accreting terrestrial planets have mixed atmospheres of H₂ and H₂O through impact degassing from planetary building blocks and gravitational capture of the surrounding nebular gas. If the conditions are right, water vapor is produced from nebula-captured atmospheres through oxidation of hydrogen by oxides at the surface (Ikoma and Genda, 2006; Kimura and Ikoma, 2020), and on the contrary, hydrogen is produced from impact-generated water vapor through chemical reduction by metallic iron in building blocks (Kuramoto and Matsui, 1996).

The effect of the radiative cooling by H_2O and chemical products from H_2 and H_2O on the hydrodynamic escape has not been fully investigated. Johnstone (2020) considered the radiative emission of H_2O in rotational bands in the escape outflows of H_2O atmospheres and indicated that the radiative cooling may have little effect on the hydrodynamic escape. However, Johnstone (2020) neglected the emission in vibrational bands: the effect of the radiative cooling by H_2O is expected to be larger when the emission in vibrational bands is taken into account because its intensity is higher than that in rotational bands in part of the temperature range of the outflows (e.g., Rothman et al., 2013). Moreover, radiatively active chemical products such as OH and H_3^+ are known to enhance the effect of the radiative cooling (Yoshida and Kuramoto, 2021). If their radiative cooling suppresses the hydrodynamic escape sufficiently, the timescale for H_2 escape is prolonged compared to that for pure hydrogen atmospheres, and the amounts of water loss and accumulated oxygen are suppressed compared to the previous estimations.

In this study, we apply our 1-D hydrodynamic escape model of multi-component atmospheres considering radiative and chemical processes developed by Yoshida and Kuramoto (2020) to H_2 - H_2O atmospheres on terrestrial planets with mass of $1M_\oplus$ around pre-main sequence M dwarfs and estimate their atmospheric escape rates. Here we consider line emission in a wide range of wavelength by radiatively active species including chemical products in the escape outflows. Then, we propose possible evolutionary tracks of H_2 - H_2O atmospheres in the runaway greenhouse state during the host-stellar pre-main sequence phase. This paper is organized as follows. In Section 2, we describe the outline of our hydrodynamic escape model. In Section 3, we show the numerical results of the atmospheric profiles, energy balance, and atmospheric escape rate. In Section 4, we discuss the difference of our results from those of Johnstone (2020) and possible atmospheric evolutionary tracks estimated from the calculated escape rate.

2. MODEL DESCRIPTION

A radially one-dimensional hydrodynamic escape model developed by Yoshida & Kuramoto (2020) is applied with some modifications to the chemical and radiative processes. The detail of the model is described in Appendix A and Yoshida & Kuramoto (2020). Below, we present the outline of the model.

We suppose a rocky planet with mass of $1M_\oplus$ orbiting at 0.02 au around an M8 dwarf with mass of $0.09 M_\odot$, the stellar properties of which are similar to those of TRAPPIST-1 (Grootel et al., 2018). The orbit of 0.02 au corresponds to the inner edge of the habitable zone during the main sequence phase of such an M8 dwarf (Kopparapu et al., 2013). The dependence of the atmospheric escape on the orbital radius is discussed later.

The gas at the bottom of the atmosphere is assumed to be composed of H_2 and H_2O . For simplicity, other components such as carbon species and nitrogen species are neglected because H_2O would dominate the atmospheric molecular species bearing heavy elements under the runaway greenhouse state referring to the volatile compositions of Earth and volatile-rich primitive meteorites, in which the amount of H_2O is larger than those of carbon and nitrogen (e.g., Marty, 2012). The lower boundary is set at $r = R_p + 1000 \text{ km}$ ($\equiv r_0$), where R_p is the radius of the planet. The number density of H_2 at the lower boundary is set at $1 \times 10^{19} \text{ m}^{-3}$ assuming the typical gas density at the altitude above which the stellar XUV irradiation is absorbed completely (e.g., Kasting et al., 1983). The number density of H_2O is given as a parameter in each simulation run. In each simulation run, the atmospheric density and temperature at the lower boundary are fixed. The temperature at the lower boundary is set at 400 K, corresponding to the skin temperature, which is the asymptotic temperature at high altitudes of the upper atmosphere. The upper boundary is set at $r = 50 R_p$. The other physical quantities at the lower and upper boundaries are estimated by linear extrapolations from the calculated domain.

The basic equations in this model are the fluid equations of continuity, momentum, and energy for a multi-component gas considering chemical and radiative processes (Appendix A1). They are solved by numerical integration about time until the physical quantities settle into their steady profiles by the same method that Yoshida & Kuramoto (2020) used (see also Appendix A4).

As for the chemical processes, 93 chemical reactions are considered for 15 atmospheric components: H_2 , H_2O , H, O, $\text{O}(^1\text{D})$, OH, O_2 , H^+ , H_2^+ , H_3^+ , O^+ , O_2^+ , OH^+ , H_2O^+ , and H_3O^+ (Table A1, A2). See Appendix A2 for the model formulation of chemical processes.

This study adopts the X-ray and UV spectrum profile from 0.1 to 280 nm estimated for the M8 dwarf TRAPPIST-1 (Peacock et al., 2019). The present total XUV flux is $1.78 \times 10^{-1} \text{ J m}^{-2} \text{ s}^{-1}$ at 0.02 au. The XUV luminosity during the pre-main sequence phase is assumed to be 0.001 times the total stellar luminosity, which is about 10-230 times the present when the stellar age is from 10 Myr to 1 Gyr (Luger and Barnes, 2015). Here we refer to Baraffe et al. (1998) for the evolution of the stellar luminosity. To calculate the profiles of heating rates and photolysis rates, we calculate the radiative transfer of parallel stellar photon beams in the spherically symmetric atmosphere by applying the method formulated by Tian et al. (2005a). Following this calculation, the spherical shell average is taken for the three-dimensional heating distribution.

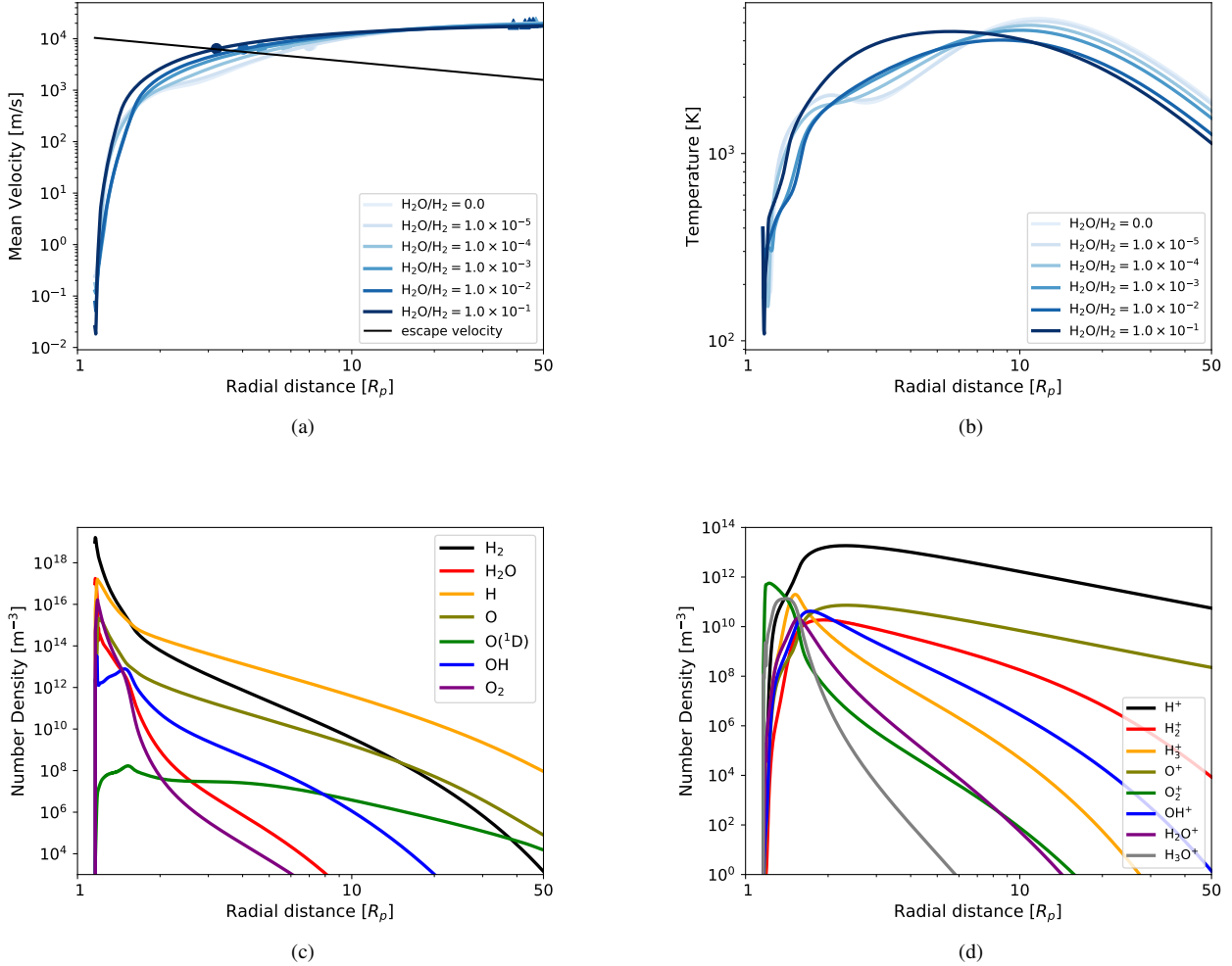


Figure 1. Atmospheric profiles when the XUV flux is 100 times the present. (a) Mean velocity for six choices of the basal H₂O/H₂ mole ratio. The dots represent the transonic points. The triangles indicate the exobase. The black line represents the local escape velocity. (b) Temperature for six basal H₂O/H₂ ratios. (c) Number density of neutral species for H₂O/H₂ = 0.01. (d) Number density of ion species for H₂O/H₂ = 0.01. The radial distance is shown in the planet radius R_p .

We consider radiative cooling by thermal line emission of H₂O, OH, H₃⁺, and OH⁺ with line data provided by HITRAN database (Rothman et al., 2013; <http://hitran.org>) and ExoMol database (Tennyson et al., 2016; <http://exomol.com>). Our model contains 5021 transitions of H₂O, 383 transitions of OH, 5200 transitions of H₃⁺, and 192 transitions of OH⁺ to cover more than 99% of the total energy emission in the temperature range of 100 - 1000 K. Then we calculate the radiative cooling rate by applying the method formulated by Yoshida & Kuramoto (2020) which includes the Doppler shift of emission line wavelength caused by outflow acceleration. See Appendix A3 for the model formulation of radiative transfer processes.

3. RESULTS

3.1. Atmospheric profiles and energy balance

The structure of steady outflows is shown in Fig. 1, which exhibits the radial profiles of mean velocity, temperature, and number densities of neutral and ion species for typical steady state solutions when the XUV flux is 100 times the present. The flow is radially accelerated from near zero velocity to supersonic in each solution (Fig. 1(a)). Molecules such as H₂ and H₂O are dissociated efficiently, and chemical products such as H, O, OH, and O₂ are produced (Fig. 1(c)). This behavior is common for other basal H₂O/H₂ cases.

The energy balance and its dependence on the basal $\text{H}_2\text{O}/\text{H}_2$ ratio in the lower region where the stellar XUV irradiation is absorbed mainly are shown in Fig. 2. The heating efficiency, η , which represents the net energy deposited as sensible heat relative to the total input of radiative energy, is given by

$$\eta = \frac{\int_{r_0}^{r_1} (q_{\text{abs}} - q_{\text{ch}} - q_{\text{rad}}) 4\pi r^2 dr}{\int_{r_0}^{r_1} q_{\text{abs}} 4\pi r^2 dr}, \quad (1)$$

where r is the radial distance from the center of the planet, r_0 is the radial distance of the lower boundary, $r_1 = 2R_p$ (R_p : planet radius), and q_{abs} , q_{ch} and q_{rad} are the radiative heating rate by UV absorption, the rate of net chemical expense of energy, and the radiative cooling rate, respectively (see Appendix). As shown in the upper panel, the total radiative cooling rate increases with the basal $\text{H}_2\text{O}/\text{H}_2$ ratio due to the increase in the abundance of coolant. Here the main coolant is H_2O . In addition, radiatively active chemical products such as OH and OH^+ enhance the energy loss via radiative cooling. As a result, the heating efficiency decreases as the basal $\text{H}_2\text{O}/\text{H}_2$ ratio increases: it becomes lower than 10 % when the basal $\text{H}_2\text{O}/\text{H}_2$ ratio ≥ 0.1 (see the lower panel in Fig. 2).

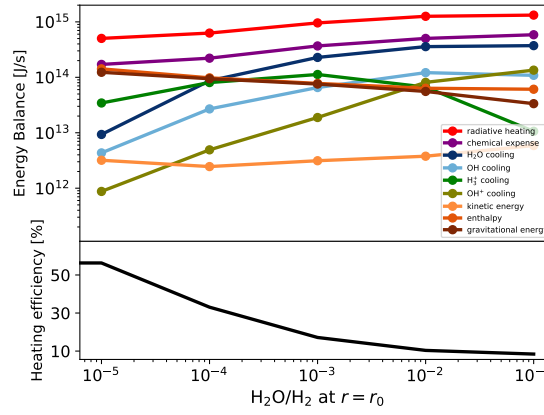


Figure 2. Energy balance in the region $r_0 \leq r \leq 2R_p$ for different values of the basal $\text{H}_2\text{O}/\text{H}_2$ mole ratio when the XUV flux is 100 times the present; R_p is the planet radius and r_0 is the radial distance of the atmospheric lower boundary ($= R_p + 1000$ km). Legends: “kinetic energy” is the flux of kinetic energy, “enthalpy” is the flux of enthalpy, “gravitational energy” is the difference of the gravitational potential, “radiative heating” is the heating rate by UV absorption, “chemical expense” is the net chemical expense of energy, and “ H_2O cooling”, “ OH cooling”, “ H_3^+ cooling” and “ OH^+ cooling” are the radiative cooling rate by H_2O , OH , H_3^+ and OH^+ respectively. The black line in the lower panel represents the heating efficiency (see Eq. (1) for its definition).

3.2. Escape rate

The atmospheric escape rate in kg/Myr is shown in Fig. 3. Here the escape rate of species i ($i = \text{H}_2$ or H_2O) is calculated by

$$F_{m,i} = 4\pi r_0^2 \rho_i(r_0) v_i(r_0), \quad (2)$$

where $\rho_i(r_0)$ and $v_i(r_0)$ are the mass density and velocity of species i at the lower boundary, respectively. In the left panel, the escape rate of H_2 is found to decrease as the basal $\text{H}_2\text{O}/\text{H}_2$ ratio increases, which is due to the decrease in the heating efficiency by the enhanced radiative cooling and the suppression of the H_2 radial velocity by H_2O drag in the outflow. It is almost one order of magnitude smaller when $\text{H}_2\text{O}/\text{H}_2 = 0.1$ than that for the pure hydrogen atmosphere.

While H_2O also escapes to space with H_2 , fractionation between H_2 and H_2O occurs significantly as the basal $\text{H}_2\text{O}/\text{H}_2$ ratio increases, as noticed from a comparison between Fig. 3(a) and (b). The dashed line in Fig. 3(a) represents the critical flux of H_2 , beyond which H_2 can drag H_2O up to outside the planetary gravitational well, given by

$$F_{\text{crit},\text{H}_2\text{O}} = \frac{4\pi r_0^2 b_{\text{H}_2,\text{H}_2\text{O}} g X_{\text{H}_2}}{k_B T} (m_{\text{H}_2\text{O}} - m_{\text{H}_2}), \quad (3)$$

where k_B is the Boltzmann constant, $m_{\text{H}_2\text{O}}$ is the molecular mass of H_2O , $b_{\text{H}_2,\text{H}_2\text{O}}$ is the binary diffusion coefficient between H_2 and H_2O , g is the gravity acceleration, and X_{H_2} is the mixing fraction of H_2 (Hunten et al., 1987). The escape rate of H_2 is found

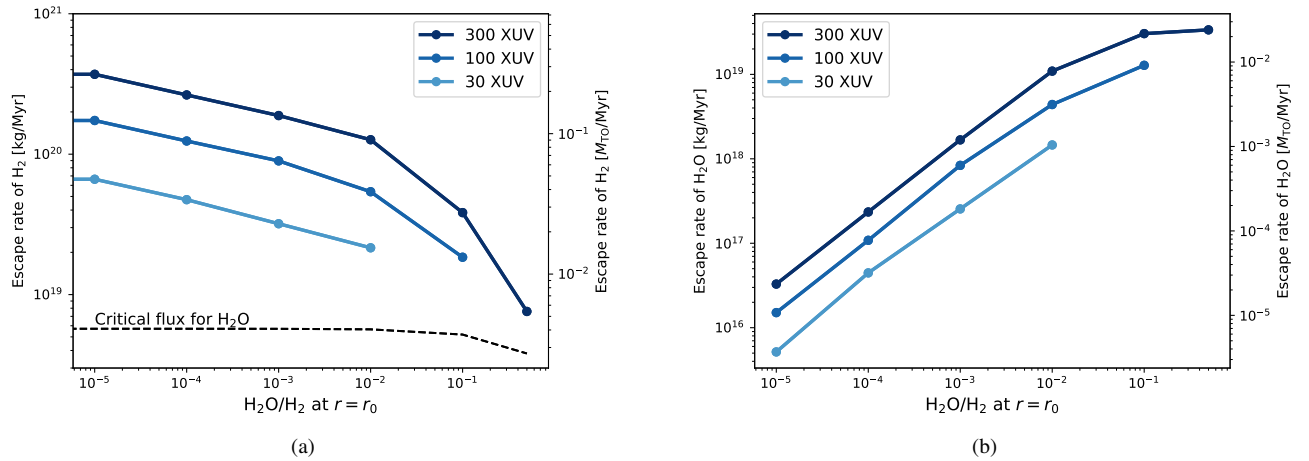


Figure 3. Escape rates of H₂ (a) and H₂O (b) in kg/Myr as functions of the basal H₂O/H₂ mole ratio for the assumed XUV fluxes 30 times (“30 XUV”), 100 times (“100 XUV”), and 300 times (“300 XUV”) the present. The right vertical axis represents the flux normalized by the mass of the present terrestrial ocean: $M_{T0} = 1.4 \times 10^{21}$ kg. The dashed line in (a) represents the critical flux of H₂ above which H₂ can drag H₂O upward.

to become close to the critical flux as the basal H₂O/H₂ ratio increases. Our numerical integration becomes unstable when the escape rate of H₂ becomes close to the critical flux. The escape rate of H₂ would continue to decrease and reach the critical flux when the H₂O/H₂ ratio becomes enough large. Under larger H₂O/H₂ ratio, no escape of H₂O would occur.

The total escape rate is also found to increase almost proportionally to the XUV flux when the basal H₂O/H₂ ratio is the same. This is because the atmospheric profile and energy balance do not change significantly with the XUV flux.

4. DISCUSSION

4.1. Comparison with the results under the settings of radiative cooling processes used by Johnstone (2020)

In this section, we compare the results shown in Section 3 with those calculated under the settings of the radiative cooling processes used by Johnstone (2020) to clarify the effects of the radiative cooling by H₂O in vibrational bands and the radiatively active chemical products that we have considered newly. Johnstone (2020) considered the radiative emission by H₂O in rotational bands formulated by Hollenbach and McKee (1979), Ly- α emission by H given by Murray-Clay et al. (2009) and Guo (2019), and emission by O at 63 and 147 μ m derived by Bates (1951). Figure 4 shows the difference in the energy balance and atmospheric escape rate between the results under the settings of radiative emission of this study and those under Johnstone’s settings. The radiative cooling rate of H₂O under our settings is larger than that under Johnstone’s settings due to the addition of the emission in vibrational bands. Moreover, the radiative emission by the chemical products that we have considered enhances the radiative cooling rate, while the emission by H and O in Johnstone’s settings has little effect on the energy balance. As a result, the heating efficiency and atmospheric escape rate under our settings become lower over the range of the atmospheric compositions that we have considered.

4.2. Evolution of H₂-H₂O atmospheres during the pre-main sequence phase

4.2.1. Changes in the amount and composition of H₂-H₂O atmospheres

In this section, we show the evolution of H₂-H₂O atmospheres in their runaway greenhouse condition during the pre-main sequence phase of the host star based on our new estimate of the atmospheric escape rate. Firstly, we consider a planet with the mass and radius same as those of the Earth, orbiting at 0.02 au around a pre-main sequence star that ends up an M8 dwarf. This orbit corresponds to the inner edge of the habitable zone after the star entered the main sequence phase, so the planet is exposed to extremely strong XUV flux during the pre-main sequence phase and moreover the duration of the runaway phase is quite long. We assume that the duration of the runaway greenhouse phase is 2 Gyr (Ramirez and Kaltenegger, 2014). The planet is assumed to be exposed to the stellar irradiation since the stellar age reaches 10 Myr when the surrounding nebular gas is expected to have dissipated (e.g., Haisch et al., 2001). The XUV flux during the pre-main sequence phase is assumed to be 0.001 times the total stellar luminosity: it decreases from 230 times to 10 times the present as the stellar age increases from 10 Myr to 1 Gyr (Fig.

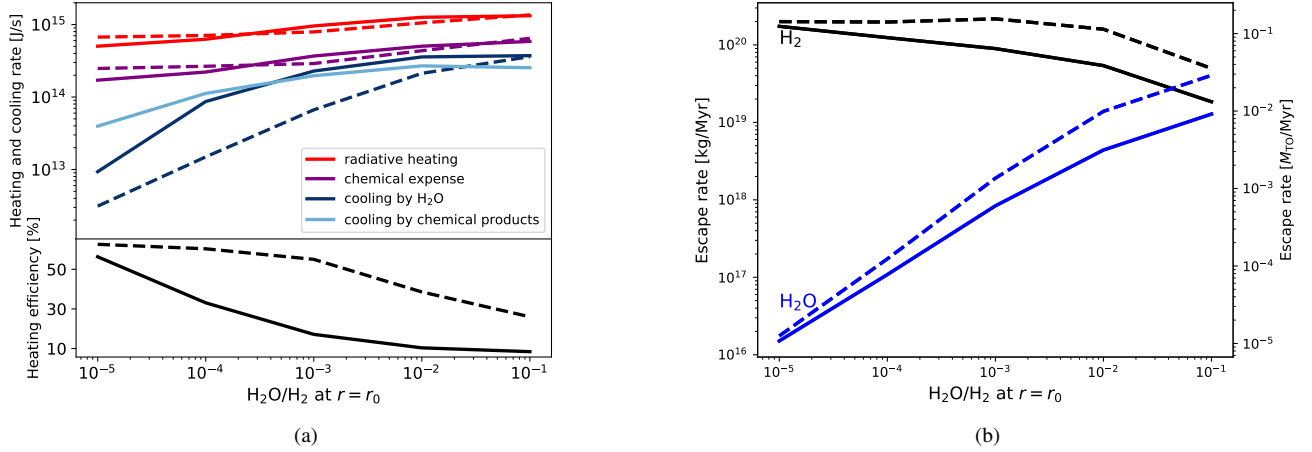


Figure 4. Radiative heating and cooling rates (upper panel) and heating efficiencies (lower panel) in the region $r_0 \leq r \leq 2R_p$ (a) and atmospheric escape rates in kg/Myr (b) as functions of the basal $\text{H}_2\text{O}/\text{H}_2$ mole ratio when the XUV flux is 100 times the present. The right vertical axis of (b) represents the flux normalized by the mass of the present terrestrial ocean: $M_{\text{TTO}} = 1.4 \times 10^{21}$ kg. The solid lines correspond to the values under the settings of radiative emission of this study, and the dashed lines correspond to those under the settings of Johnstone (2020).

1 in Luger and Barnes, 2015). The lower atmosphere is assumed to be composed of H_2 and H_2O . The mixing ratio $\text{H}_2\text{O}/\text{H}_2$ and the initial atmospheric amount are taken to be parameters because of the uncertainty in the origin and supply of volatiles. For simplicity, we neglect other atmospheric escape processes, volatile delivery, and interaction between the atmosphere and the planetary surface during the hydrodynamic escape. The composition at the lower boundary of the upper escaping atmosphere is assumed to be equal to the composition at the surface. Once the H_2 escape flux reaches the critical flux for H_2O (see Eq. 3), we stop the H_2O escape and consider diffusion-limited escape for H_2 . As mentioned, however, we cannot find the solution with the H_2 escape flux equal to the critical flux, because of numerical instability; instead, we extrapolate the highest value of the $\text{H}_2\text{O}/\text{H}_2$ ratio at which we could find the solution toward higher values (namely, extending the solid lines to find the crossover point with the dashed line in Fig. 3).

Examples of atmospheric evolutionary tracks are shown in Fig. 5. The atmospheric mass of each species is expressed by the mass of the present terrestrial ocean: $M_{\text{TTO}} = 1.4 \times 10^{21}$ kg. The amount of H_2 decreases with time gradually. On the other hand, the decrease in the amount of H_2O stops, when the H_2 escape flux reaches the critical flux for H_2O . In some cases, both H_2 and H_2O are left behind when the runaway greenhouse phase ends (≈ 2000 Myr), indicating that an ocean is formed and an H_2 -rich atmosphere remains after the star entered the main sequence phase.

The timescale for H_2 escape and the final H_2O amount are shown as functions of the initial atmospheric amounts of H_2 and H_2O in Fig. 6. Here we define the timescale for H_2 escape as the time for the amount of H_2 to reach $1.0 \times 10^{-3} M_{\text{TTO}}$. As seen in Fig. 6(a), the timescale for H_2 escape becomes longer as the initial $\text{H}_2\text{O}/\text{H}_2$ ratio increases. This is due to the suppression of the atmospheric escape by the radiative cooling and the decrease in the diffusion velocity of H_2 . The final H_2O amount also increases as the initial $\text{H}_2\text{O}/\text{H}_2$ ratio increases (Fig. 6(b)). The timescale for H_2 escape exceeds the duration of the runaway greenhouse phase and, thus, part of H_2O is left behind in a wide range of initial atmospheric amounts.

The formation of such massive H_2 - H_2O atmospheres that we have considered here could occur depending on planetary accretion processes, nebular properties, and so on. If a proto-planet reaches a mass of $\sim 1M_{\oplus}$ before the protoplanetary nebula dissipates, it can capture the surrounding nebular gas with more than $\sim 10M_{\text{TTO}}$ (e.g., Ikoma and Genda, 2006). Moreover, the mass of the nebula-captured atmosphere may increase significantly when the atmospheric mean molecular weight and effective specific heat increase by mixing of high-molecular-weight components such as H_2O (Kimura and Ikoma, 2020). In addition, volatile-rich planetary building blocks like carbonaceous chondrites could also deliver volatiles although their amounts are highly uncertain.

Figure 7 is the same as Fig. 6 but for the planetary orbital radius of 0.05 au, which corresponds to the outer edge of the habitable zone around M8 dwarfs (Luger and Barnes, 2015). In this case, H_2 and H_2O tend to be left behind after the runaway greenhouse phase compared with the planet in the inner edge of the habitable zone because the incident XUV flux is smaller and the duration

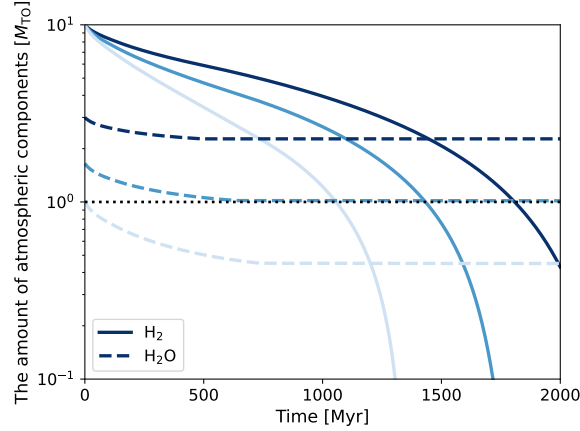


Figure 5. Changes in the atmospheric amounts of H₂ and H₂O with time. The vertical axis represents the atmospheric mass of each species normalized by the mass of the present terrestrial ocean: $M_{\text{TO}} = 1.4 \times 10^{21}$ kg. The solid lines and dashed lines represent the amounts of H₂ and H₂O, respectively. The initial amount of H₂ is $10M_{\text{TO}}$, and the initial amounts of H₂O are $1M_{\text{TO}}$, $1.7M_{\text{TO}}$, $3M_{\text{TO}}$, respectively.

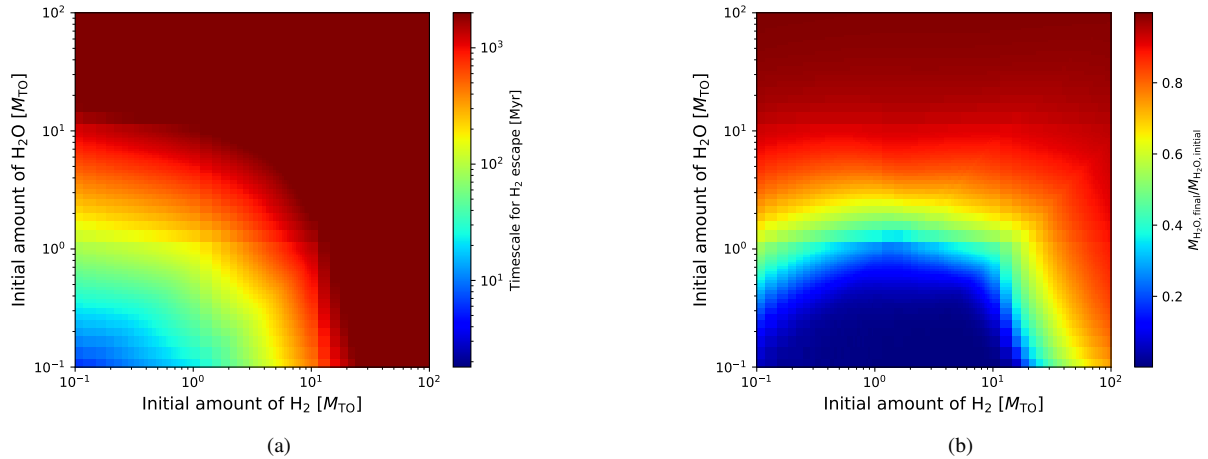


Figure 6. Timescale for H₂ escape (a) and the final H₂O amount relative to its initial amount (b) as functions of the initial amounts of H₂ and H₂O on the planet of $1M_{\oplus}$ orbiting at 0.02 au. The duration of the runaway greenhouse phase is assumed to be 2 Gyr.

of the runaway greenhouse condition is shorter (~ 0.1 Gyr; Luger and Barnes, 2015). Planets around more massive M dwarfs are also likely easy to keep H₂ and H₂O until the runaway greenhouse condition ends for the same reason.

4.2.2. Other processes affecting the estimation of atmospheric evolution

In this study, we consider only H₂, H₂O, and their chemical products as the atmospheric components for simplicity. Qualitatively, considering other components such as carbon species leads to a decrease in the atmospheric escape rate by their strong radiative cooling (Yoshida and Kuramoto, 2020; 2021). Moreover, radiatively active ions such as H⁻ and H₃O⁺ could enhance the effect of the radiative cooling (e.g., Lenzuni et al., 1991; Yurchenko et al., 2020). Quantitative investigation of their effects is beyond the scope of this study.

We neglect interaction between the atmosphere and the planetary surface. Planets with runaway greenhouse atmospheres are predicted to have magma oceans (e.g., Hamano et al., 2013; Lebrun et al., 2013). In that case, if material circulation and mixing occur efficiently both in the atmosphere and magma ocean, the atmospheric composition is buffered by the redox state of the mantle (e.g., Holland, 1984). It is our future work to consider the effects of the interaction between the atmosphere and surface on the atmospheric evolution.

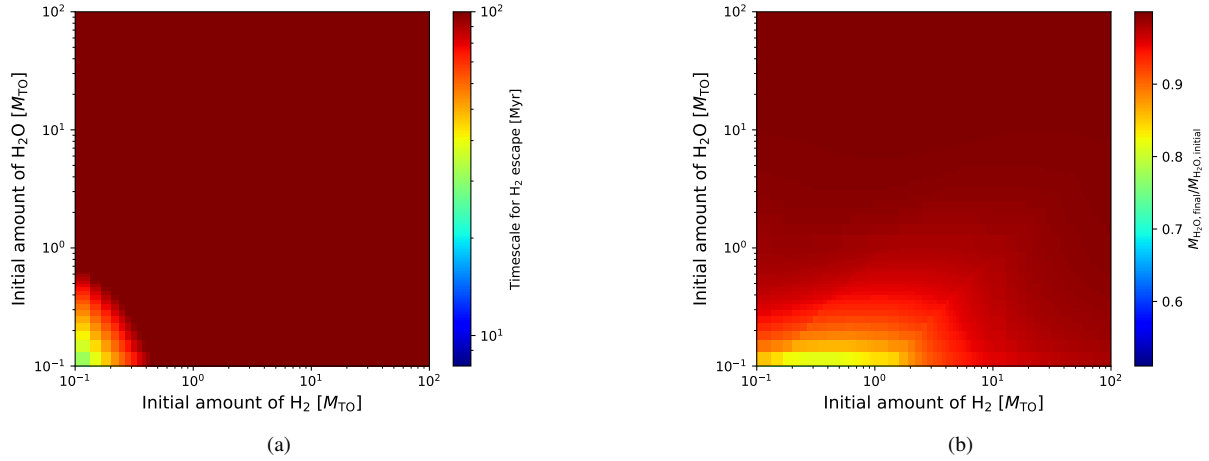


Figure 7. Same as Fig. 6 but for the planet orbiting at 0.05 au. The duration of the runaway greenhouse phase is assumed to be 0.1 Gyr.

We assume that the atmospheric composition at the lower boundary in the calculations is equal to the composition at the surface. However, chemical processes in the lower and middle atmosphere could change the composition at the bottom of the escaping upper atmosphere from that at the surface. Part of H_2O is expected to be dissociated by photolysis in the stratosphere (e.g., Hunten and Strobel, 1974), which leads to decreasing the mixing ratio of H_2O in the escape outflow, and increasing the efficiency of H_2 escape.

Provided the H_2O -dominated atmosphere is kept in a moist/runaway-greenhouse condition, the remaining H_2O would continue to be lost through its photolysis followed by escape of hydrogen produced from H_2O . This process may have also been important for water loss from Venus. Our model estimates that H_2 is lost almost completely in ~ 1 Gyr from an H_2 - H_2O atmosphere, if the planet has been located at the current location of Venus from a Sun-like young star and the initial atmospheric mass is a few times as massive as the present-day Earth’s oceans. Given that Venus is expected to have been in a moist/runaway-greenhouse condition, it can lose H_2O completely in the remaining ~ 3 Gyr (e.g., Kasting et al., 1993; Hamano et al., 2013). This is a clear contrast to terrestrial planets currently orbiting in the habitable zones around M dwarfs, which ended the moist/runaway-greenhouse condition, leaving H_2O due to cold trap at the time when their host stars entered the main sequence phase. According to classic models (e.g., Hunten, 1973; Kasting et al., 1993), the timescale for the complete loss of H_2O with initial amount equivalent to that of the present-day Earth’s oceans is several hundred million years, provided H_2O is a major component in the atmosphere and hydrogen produced from H_2O escapes to space in a diffusion-limited fashion. On the other hand, a large amount of oxygen produced from photolysis of H_2O may be left and accumulated in the remaining atmosphere, leading to a significant reduction in the diffusion velocity and, thus, the escape rate of hydrogen. Further investigation of the escape process of the H_2O -dominated atmosphere is needed.

4.2.3. Implication for habitability of planets around M dwarfs

Previous studies for the evolution of pure H_2O atmospheres of Earth-mass rocky planets orbiting pre-main sequence M dwarfs showed that several times the amount of Earth’s seawater is lost and massive O_2 could be produced photochemically (e.g., Luger and Barnes, 2015). The planetary desiccation could severely hamper the ability of life to originate and evolve on planets. Moreover, oxidizing environments could also prevent the emergence of life organisms because prebiotic chemistry needs reducing environments (e.g., Schlesinger and Miller, 1983). Therefore, their results indicated that terrestrial planets around M dwarfs are not suitable for the origin and evolution of life.

By contrast, our results indicate that both H_2 and H_2O can survive during the early runaway greenhouse phase and H_2 -rich environments with oceans could be formed after the end of the runaway greenhouse phase. Such reducing environments are suitable for photochemical production of organic matters potentially linked to the emergence of living organisms (e.g., Schlesinger and Miller, 1983). Therefore, some planets in the habitable zones around M dwarfs may have temperate and reducing surface environments suitable for the origin of life.

5. CONCLUSION

We have applied our 1-D hydrodynamic escape model to an H₂-H₂O atmosphere on a planet with mass of $1M_{\oplus}$ around a pre-main sequence M dwarf. According to our results, the atmospheric escape rate decreases with the basal H₂O/H₂ ratio because of the energy loss by the radiative cooling of H₂O and chemical products such as OH and H₃⁺. The escape rate of H₂ becomes one order of magnitude smaller when the basal H₂O/H₂ = 0.1 than that of the pure hydrogen atmosphere. The timescale for H₂ escape could exceed the duration of the early runaway phase depending on the initial atmospheric amount and composition. Our results suggest that temperate and reducing environments with oceans which are suitable for the origin of life could be formed after the end of the runaway greenhouse phase on terrestrial planets around M dwarfs.

ACKNOWLEDGEMENTS

We thank an anonymous reviewer whose comments greatly improved the manuscript. This work was supported by MEXT/JSPS KAKENHI Grant Number 18H05439. N. T. was also supported by JSPS KAKENHI Grant Number 18KK0093, 19H00707, 20H00192, and 22H00164. M. I. was also supported by JSPS KAKENHI Grant Number JP21H01141. K. K. was also supported by MEXT/JSPS KAKENHI Grant Number 17H06457 and 21K03638.

APPENDIX

A. DETAILS OF THE MODEL

A.1. Basic equations

We have solved the equations of continuity, momentum and energy for a multi-component gas assuming spherical symmetry,

$$\frac{\partial n_i}{\partial t} + \frac{1}{r^2} \frac{\partial(n_i u_i r^2)}{\partial r} = \omega_i, \quad (\text{A1})$$

$$\frac{\partial u_i}{\partial t} + u_i \frac{\partial u_i}{\partial r} = -\frac{1}{\rho_i} \frac{\partial p_i}{\partial r} - \frac{GM}{r^2} + \sum_j (u_j - u_i) \frac{n_j}{m_i} \mu_{ij} k_{ij}, \quad (\text{A2})$$

$$\frac{\partial}{\partial t} \left[\rho \left(\frac{1}{2} u^2 + E \right) \right] + \frac{1}{r^2} \frac{\partial}{\partial r} \left\{ \left[\left(\frac{1}{2} u^2 + E + \frac{p}{\rho} \right) \rho u \right] r^2 \right\} = -\frac{GM}{r^2} \rho u + q, \quad (\text{A3})$$

where t is the time, r is the distance from the planet's center, n_i , ρ_i , u_i , p_i , and ω_i are the number density, mass density, velocity, partial pressure, and production rate of species i , respectively, G is the gravitational constant, M is the mass of the planet, ρ , p , and E are the total mass density, total pressure, and total specific internal energy, respectively, u is the mean gas velocity, μ_{ij} is the reduced molecular mass between species i and j , k_{ij} is the momentum transfer collision frequency that follows

$$k_{ij} = \frac{k_B T}{\mu_{ij} b_{ij}}, \quad (\text{A4})$$

where k_B is the Boltzmann constant, T is the temperature and b_{ij} is the binary diffusion coefficient, which is given by (Zahnle et al., 1990)

$$b_{ij} = \begin{cases} 1.96 \times 10^6 \frac{T^{1/2}}{\mu_{ij}} & \text{for neutral-neutral pair} \\ 4.13 \times 10^{-8} \frac{T}{\mu_{ij}^{1/2} \alpha^{1/2}} & \text{for neutral-ion pair} \\ 8.37 \times 10^{-5} \frac{T^{5/2}}{\mu_{ij}^{1/2}} & \text{for ion-ion pair} \end{cases} \quad (\text{A5})$$

where α is the polarizability (Banks and Kockarts, 1973; Garcia, 2007). Here, b_{ij} , T , μ_{ij} and α are expressed in cm⁻¹s⁻¹, K, g and cm³, respectively. The total internal energy is given by

$$\rho E = \frac{1}{n} \left(\sum_i \frac{n_i}{\gamma_i - 1} \right) p, \quad (\text{A6})$$

where γ_i is the ratio of specific heat of species i . The net heating rate is given by

$$q = q_{\text{abs}} - q_{\text{ch}} - q_{\text{rad}}, \quad (\text{A7})$$

where q_{abs} is the heating rate by XUV absorption (see A.3), q_{ch} is the rate of net chemical expense of energy (see A.2), and q_{rad} is the radiative cooling rate by infrared active molecules (see A.3).

A.2. Chemical processes

A total of 93 chemical reactions are considered for 15 atmospheric components: H_2 , H_2O , H , O , $\text{O}(^1\text{D})$, OH , O_2 , H^+ , H_2^+ , H_3^+ , O^+ , O_2^+ , OH^+ , H_2O^+ , and H_3O^+ (Table A1).

The photolysis rate $f_{\text{ph},i}$ is given by

$$f_{\text{ph},i} = \int_{\lambda} n_i \sigma_i(\lambda) I(\lambda) d\lambda, \quad (\text{A8})$$

where $\sigma_i(\lambda)$ is the photodissociation/photoionization cross section at wavelength λ for species i and $I(\lambda)$ is the incident XUV photon flux at wavelength λ . The energy consumed per unit time by this photolysis $q_{\text{ph},i}$ is given by

$$q_{\text{ph},i} = f_{\text{ph},i} \frac{hc}{\lambda_{\text{th},i}}, \quad (\text{A9})$$

where $\lambda_{\text{th},i}$ is the threshold wavelength for the photolysis of species i , h is the Planck constant, and c is the speed of light in vacuum. We adopt the photodissociation and photoionization cross sections provided by ‘‘PHoto Ionization/Dissociation RATES’’ (Huebner and Mukherjee, 2015; <http://phidrates.space.swri.edu>).

In addition to photolysis reactions, this study considers bimolecular reactions. The bimolecular reaction rate f_{R} can be written as

$$f_{\text{R}} = k_{\text{R}} n_i n_j, \quad (\text{A10})$$

where n_i and n_j represent the number densities of reactant i and j , respectively, and k_{R} is the corresponding reaction rate coefficient. We use the reaction rate coefficients provided by ‘‘The UMIST Database for Astrochemistry 2012’’ (McElroy et al., 2013; <http://udfa.ajmarkwick.net>). We neglect the formation of molecules that have more than one carbon because of low gas densities in the atmospheric regions where the outflow to space accelerates. The energy consumed per unit time by the bimolecular reaction is given by

$$q_{\text{R}} = -f_{\text{R}} \Delta E_{\text{R}}, \quad (\text{A11})$$

where ΔE_{R} is the heat of reaction, which is positive for endothermic reactions and negative for exothermic reactions. In the evaluation of the heats of reaction, we make use of the enthalpies of formation listed in Le Teuff et al. (2000). The energy consumption rate q_{ch} is calculated by summing the consumed amounts of energy by individual chemical reactions including photolysis.

A.3. Radiative processes

In order to calculate the radial profiles of heating rates and photolysis rates in the atmosphere, we model the radiative transfer of parallel stellar photon beams in a spherically symmetric atmosphere by applying the method formulated by Tian et al. (2005a). We consider the XUV absorption by H_2 , H_2O , H , O , OH , and O_2 . The stellar beam is assumed to be absorbed by the Beer’s law. The energy deposition in a given layer along each path is then multiplied by the area of the ring (Fig. 6 in Tian et al., 2005a) to obtain the total energy deposited into the shell segment. The heating rate q_{abs} is given by the total energy absorbed per unit time by each shell divided by the volume of the shell. We adopt the X-ray and UV spectrum from 0.1 to 280 nm estimated for TRAPPIST-1 by Peacock et al. (2019), and assume that the ratio of the XUV luminosity to the total stellar luminosity is 10^{-3} during the pre-main sequence phase.

We consider radiative cooling by thermal line emission of H_2O , OH , H_3^+ , and OH^+ . The radiative cooling rate due to a transition from energy level i to j of radiatively active molecular species s is given by

$$q_{\text{rad},s,ij} = n_{s,i} A_{ij} h\nu_{ij} \beta_{ij}, \quad (\text{A12})$$

where $n_{s,i}$ is the population density in level i , A_{ij} is the spontaneous transition probability, $h\nu_{ij}$ is the energy difference between level i and level j , and β_{ij} is the photon escape probability. The total radiative cooling rate by species s is calculated by summing the radiative cooling rates by all the transitions. The population density $n_{s,i}$ is calculated under the assumption of LTE as

$$n_{s,i} = n_s \frac{g_i}{Z} \exp\left(-\frac{E_i}{k_{\text{B}}T}\right) \quad (\text{A13})$$

where n_s and Z are the total number density and partition function of species s , and g_i and E_i are the statistical weight and energy of level i . Approximating that half of the photons are emitted outward while the other half is emitted downward and then absorbed by dense, lower atmospheric layers, the bulk escape probability is evaluated by

$$\beta(r) = \frac{1}{2} \int_0^{\infty} \phi(\nu, r) \exp\left[-\int_{r_{\text{top}}}^r \alpha_{\text{L}} \phi(\nu, r) dr\right] d\nu \quad (\text{A14})$$

where r_{top} is the radius of the outer boundary (the top of the atmosphere), α_L is the integrated absorption coefficient, and $\phi(\nu, r)$ is the line profile, α_L is given by

$$\alpha_L = \frac{c^2}{8\pi\nu_{ij}^2} n_{s,i} A_{ij} \left(\frac{n_{s,j} g_i}{n_{s,i} g_j} - 1 \right). \quad (\text{A15})$$

Assuming the Doppler profile, $\phi(\nu, r)$ is given by

$$\phi(\nu, r) = \frac{1}{\sqrt{\pi}\Delta\nu_D} \exp \left[-\frac{1}{(\Delta\nu_D)^2} \left(\nu - \nu_0 - \frac{u_s(r)}{c} \nu_0 \right)^2 \right], \quad (\text{A16})$$

where $u_s(r)$ is the velocity profile of radiative sources and ν_0 is the central frequency of the line profile under no flow; $\Delta\nu_D$ is the Doppler width given by

$$\Delta\nu_D = \frac{\nu_0}{c} \sqrt{\frac{3k_B T}{m_s}}, \quad (\text{A17})$$

where m_s is the molecular mass of species s . The net radiative cooling rate q_{rad} is obtained by the sum of contributions by H₂O, OH, H₃⁺, and OH⁺. We use the line data provided by HITRAN database (Rothman et al., 2013; <http://hitran.org>) and ExoMol database (Tennyson et al., 2016; <http://exomol.com>). We consider 5021 transitions of H₂O, 383 transitions of OH, 5200 transitions of H₃⁺, and 192 transitions of OH⁺ to cover more than 99% of the total energy emission in the temperature range of 100 - 1000 K.

A.4. Calculation method

The basic equations are solved by numerical time integration until the physical quantities settle into their steady profiles. These equations can be split into advection phases and nonadvection phases. We employ the CIP method to solve the advection phases (Yabe and Aoki, 1991) to keep numerical stability and accuracy for hydrodynamic escape simulations (Kuramoto et al., 2013). After solving the advection phases, we solve the nonadvection phases with a finite-difference approach. The nonadvection phases of the energy equation are solved explicitly. Those of the continuity equations are solved with the semi-implicit method. Those of the momentum equations are solved implicitly using the quantities for the next time step that are obtained by the integration of the energy equation and the continuity equations.

On radial coordinate, 1000 numerical grids are taken with the grid-to-grid intervals exponentially increasing with r . The time step is defined so as to satisfy the CFL condition. For each parameter setup, we continue the time integration until reaching the steady state using the convergence condition described in Tian et al. (2005a).

The upper boundary is set at $r = 50 R_p$, where R_p is the radius of the planet. The lower boundary is set at $r = R_p + 1000$ km. In each simulation run, the atmospheric density and temperature at the lower boundary are fixed. We assume that only H₂ and H₂O exist at the lower boundary. The number density of H₂ at the lower boundary is set at $1 \times 10^{19} \text{ m}^{-3}$. The number density of H₂O is given as a parameter in each simulation run. The temperature at the lower boundary is set at 400 K, corresponding to the skin temperature, which is the asymptotic temperature at high altitudes of the upper atmosphere. The other physical quantities at the lower and upper boundaries are estimated by linear extrapolations from the calculated domain. As the initial condition, we use the steady profiles of the pure hydrogen atmosphere and add H₂O whose number density profiles are given by the hydrostatic structure. The initial velocities of H₂O is set at $1 \times 10^{-5} \text{ m/s}$.

REFERENCES

- Banks, P. M., & Kockarts, G. (2013). *Aeronomy. Part B*. Academic Press. San Diego
- Bates, D. R. (1951). The temperature of the upper atmosphere. *Proceedings of the Physical Society. Section B*, 64(9), 805.
- Baraffe, I., Chabrier, G., Allard, F., & Hauschildt, P. (1998). Evolutionary models for solar metallicity low-mass stars: mass-magnitude relationships and color-magnitude diagrams. arXiv preprint astro-ph/9805009.
- Bolmont, E., Selsis, F., Owen, J. E., Ribas, I., Raymond, S. N., Lecante, J., & Gillon, M. (2017). Water loss from terrestrial planets orbiting ultracool dwarfs: implications for the planets of TRAPPIST-1. *Monthly Notices of the Royal Astronomical Society*, 464(3), 3728-3741.
- Bourrier, V., De Wit, J., Bolmont, E., Stamenkovic, V., Wheatley, P. J., Burgasser, A. J., ... & Van Grootel, V. (2017). Temporal evolution of the high-energy irradiation and water content of TRAPPIST-1 exoplanets. *The Astronomical Journal*, 154(3), 121.

Table 1. Chemical reactions

No.	Reaction		Reaction rate $\text{cm}^3 \text{s}^{-1}$
R1	$\text{H}_2 + h\nu$	$\rightarrow \text{H} + \text{H}$	
R2		$\rightarrow \text{H}_2^+ + \text{e}$	
R3		$\rightarrow \text{H}^+ + \text{H} + \text{e}$	
R4	$\text{H}_2\text{O} + h\nu$	$\rightarrow \text{H} + \text{OH}$	
R5		$\rightarrow \text{H}_2 + \text{O}(^1\text{D})$	
R6		$\rightarrow \text{O} + \text{H} + \text{H}$	
R7		$\rightarrow \text{OH}^+ + \text{H} + \text{e}$	
R8		$\rightarrow \text{O}^+ + \text{H}_2 + \text{e}$	
R9		$\rightarrow \text{H}^+ + \text{OH} + \text{e}$	
R10		$\rightarrow \text{H}_2\text{O}^+ + \text{e}$	
R11	$\text{H} + h\nu$	$\rightarrow \text{H}^+ + \text{e}$	
R12	$\text{O} + h\nu$	$\rightarrow \text{O}^+ + \text{e}$	
R13	$\text{OH} + h\nu$	$\rightarrow \text{O} + \text{H}$	
R14		$\rightarrow \text{OH}^+ + \text{e}$	
R15		$\rightarrow \text{O}(^1\text{D}) + \text{H}$	
R16	$\text{O}_2 + h\nu$	$\rightarrow \text{O} + \text{O}$	
R17		$\rightarrow \text{O} + \text{O}(^1\text{D})$	
R18		$\rightarrow \text{O}^+ + \text{O} + \text{e}$	
R19		$\rightarrow \text{O}_2^+ + \text{e}$	
R20	$\text{H}_2 + \text{H}_2$	$\rightarrow \text{H}_2 + \text{H} + \text{H}$	$1.0 \times 10^{-8} \exp(-84000/T)$
R21	$\text{H}_2 + \text{H}_2\text{O}$	$\rightarrow \text{OH} + \text{H}_2 + \text{H}$	$5.8 \times 10^{-9} \exp(-52900/T)$
R22	$\text{H}_2 + \text{O}_2$	$\rightarrow \text{O} + \text{O} + \text{H}_2$	$6.0 \times 10^{-9} \exp(-52300/T)$
R23	$\text{H}_2 + \text{O}_2$	$\rightarrow \text{OH} + \text{OH}$	$3.16 \times 10^{-10} \exp(-21890/T)$
R24	$\text{H}_2 + \text{OH}$	$\rightarrow \text{O} + \text{H}_2 + \text{H}$	$6.0 \times 10^{-9} \exp(-50900/T)$
R25	$\text{H}_2 + \text{H}$	$\rightarrow \text{H} + \text{H} + \text{H}$	$4.67 \times 10^{-7} (T/300)^{-1} \exp(-55000/T)$
R26	$\text{H}_2 + \text{H}_2^+$	$\rightarrow \text{H}_3^+ + \text{H}$	2.08×10^{-9}
R27	$\text{H}_2 + \text{H}_2\text{O}^+$	$\rightarrow \text{H}_3\text{O}^+ + \text{H}$	6.40×10^{-10}
R28	$\text{H}_2 + \text{O}^+$	$\rightarrow \text{OH}^+ + \text{H}$	1.70×10^{-9}
R29	$\text{H}_2 + \text{OH}^+$	$\rightarrow \text{H}_2\text{O}^+ + \text{H}$	1.01×10^{-9}
R30	$\text{H}_2 + \text{O}$	$\rightarrow \text{OH} + \text{H}$	$3.14 \times 10^{-13} (T/300)^{2.7} \exp(-3150/T)$
R31	$\text{H}_2 + \text{OH}$	$\rightarrow \text{H}_2\text{O} + \text{H}$	$2.05 \times 10^{-12} (T/300)^{1.52} \exp(-1736/T)$
R32	$\text{H}_2 + \text{O}(^1\text{D})$	$\rightarrow \text{H} + \text{OH}$	1.0×10^{-9}
R33	$\text{H}_2\text{O} + \text{H}$	$\rightarrow \text{OH} + \text{H} + \text{H}$	$5.80 \times 10^{-9} \exp(-52900/T)$
R34	$\text{H}_2\text{O} + \text{H}^+$	$\rightarrow \text{H}_2\text{O}^+ + \text{H}$	$6.90 \times 10^{-9} (T/300)^{-0.5}$
R35	$\text{H}_2\text{O} + \text{H}_2^+$	$\rightarrow \text{H}_2\text{O}^+ + \text{H}_2$	$3.90 \times 10^{-9} (T/300)^{-0.5}$
R36	$\text{H}_2\text{O} + \text{O}^+$	$\rightarrow \text{H}_2\text{O}^+ + \text{O}$	$3.20 \times 10^{-9} (T/300)^{-0.5}$
R37	$\text{H}_2\text{O} + \text{OH}^+$	$\rightarrow \text{H}_2\text{O}^+ + \text{OH}$	$1.59 \times 10^{-9} (T/300)^{-0.5}$
R38	$\text{H}_2\text{O} + \text{H}_2^+$	$\rightarrow \text{H}_3\text{O}^+ + \text{H}$	$3.40 \times 10^{-9} (T/300)^{-0.5}$
R39	$\text{H}_2\text{O} + \text{H}_2\text{O}^+$	$\rightarrow \text{H}_3\text{O}^+ + \text{OH}$	$2.10 \times 10^{-9} (T/300)^{-0.5}$
R40	$\text{H}_2\text{O} + \text{H}_3^+$	$\rightarrow \text{H}_3\text{O}^+ + \text{H}_2$	$5.90 \times 10^{-9} (T/300)^{-0.5}$
R41	$\text{H}_2\text{O} + \text{OH}^+$	$\rightarrow \text{H}_3\text{O}^+ + \text{O}$	$1.30 \times 10^{-9} (T/300)^{-0.5}$
R42	$\text{H}_2\text{O} + \text{H}$	$\rightarrow \text{OH} + \text{H}_2$	$1.59 \times 10^{-11} (T/300)^{1.2} \exp(-9600/T)$
R43	$\text{H}_2\text{O} + \text{O}$	$\rightarrow \text{OH} + \text{OH}$	$1.85 \times 10^{-11} (T/300)^{0.95} \exp(-8571/T)$
R44	$\text{H} + \text{OH}$	$\rightarrow \text{O} + \text{H} + \text{H}$	$6.00 \times 10^{-9} \exp(-50900/T)$
R45	$\text{H} + \text{H}_2^+$	$\rightarrow \text{H}_2 + \text{H}^+$	6.40×10^{-10}
R46	$\text{H} + \text{O}^+$	$\rightarrow \text{O} + \text{H}^+$	$5.66 \times 10^{-10} (T/300)^{0.36} \exp(8.6/T)$
R47	$\text{H} + \text{H}^+$	$\rightarrow \text{H}_2^+$	$1.15 \times 10^{-18} (T/300)^{1.49} \exp(-228/T)$
R48	$\text{H} + \text{O}_2$	$\rightarrow \text{O} + \text{O} + \text{H}$	$6.0 \times 10^{-9} \exp(-52300/T)$
R49	$\text{H} + \text{O}_2$	$\rightarrow \text{OH} + \text{O}$	$2.61 \times 10^{-10} \exp(-8156/T)$
R50	$\text{H} + \text{O}$	$\rightarrow \text{OH}$	$9.90 \times 10^{-19} (T/300)^{-0.38}$

Ref. McElroy et al. (2013)

Table 2. Chemical reactions

No.	Reaction	Reaction rate cm ³ s ⁻¹
R51	H + OH → H ₂ O	$5.26 \times 10^{-18} (T/300)^{-5.22} \exp(-90/T)$
R52	H + OH → O + H ₂	$6.99 \times 10^{-14} (T/300)^{2.8} \exp(-1950/T)$
R53	O + H ⁺ → O ⁺ + H	$6.86 \times 10^{-10} (T/300)^{0.26} \exp(-224.3/T)$
R54	O + H ₂ ⁺ → OH ⁺ + H	1.50×10^{-9}
R55	O + H ₃ ⁺ → H ₂ O ⁺ + H	$3.42 \times 10^{-10} (T/300)^{-0.16} \exp(-1.4/T)$
R56	O + H ₃ ⁺ → OH ⁺ + H ₂	$7.98 \times 10^{-10} (T/300)^{-0.16} \exp(-1.4/T)$
R57	O + H ₂ O ⁺ → O ₂ ⁺ + H ₂	4.0×10^{-11}
R58	O + OH ⁺ → O ₂ ⁺ + H	7.10×10^{-10}
R59	O + OH → O ₂ + H	$3.69 \times 10^{-11} (T/300)^{-0.27} \exp(-12.9/T)$
R60	O + O → O ₂	$4.9 \times 10^{-20} (T/300)^{1.58}$
R61	O(¹ D) → O	1.0×10^{-4}
R62	O(¹ D) + H ₂ O → OH + OH	2.2×10^{-9}
R63	O(¹ D) + H ₂ → H + OH	1.0×10^{-9}
R64	O(¹ D) + O ₂ → O ₂ + O	$3.2 \times 10^{-11} \exp(70/T)$
R65	O(¹ D) + O → O + O	8.0×10^{-12}
R66	OH + H ⁺ → OH ⁺ + H	$2.1 \times 10^{-9} (T/300)^{-0.5}$
R67	OH + H ₂ ⁺ → OH ⁺ + H ₂	$7.6 \times 10^{-10} (T/300)^{-0.5}$
R68	OH + O ⁺ → OH ⁺ + O	$3.6 \times 10^{-10} (T/300)^{-0.5}$
R69	OH + H ₂ ⁺ → H ₂ O ⁺ + H	$7.6 \times 10^{-10} (T/300)^{-0.5}$
R70	OH + H ₃ ⁺ → H ₂ O ⁺ + H ₂	$1.3 \times 10^{-9} (T/300)^{-0.5}$
R71	OH + O ⁺ → O ₂ ⁺ + H	$3.6 \times 10^{-10} (T/300)^{-0.5}$
R72	OH + OH ⁺ → H ₂ O ⁺ + O	$7.0 \times 10^{-10} (T/300)^{-0.5}$
R73	OH + H ₂ O ⁺ → H ₃ O ⁺ + O	$6.9 \times 10^{-10} (T/300)^{-0.5}$
R74	OH + OH → H ₂ O + O	$1.65 \times 10^{-12} (T/300)^{1.14} \exp(-50/T)$
R75	O ₂ + H ⁺ → O ₂ ⁺ + H	2.0×10^{-9}
R76	O ₂ + H ₂ ⁺ → O ₂ ⁺ + H ₂	8.0×10^{-10}
R77	O ₂ + H ₂ O ⁺ → O ₂ ⁺ + H ₂ O	4.6×10^{-10}
R78	O ₂ + O ⁺ → O ₂ ⁺ + O	1.9×10^{-11}
R79	O ₂ + OH ⁺ → O ₂ ⁺ + OH	5.9×10^{-10}
R80	H ⁺ + e → H + PHOTON	$3.5 \times 10^{-12} (T/300)^{-0.75}$
R81	H ₂ ⁺ + e → H + H	$1.6 \times 10^{-8} (T/300)^{-0.43}$
R82	H ₃ ⁺ + e → H ₂ + H	$2.34 \times 10^{-8} (T/300)^{-0.52}$
R83	H ₃ ⁺ + e → H + H + H	$4.36 \times 10^{-8} (T/300)^{-0.52}$
R84	O ⁺ + e → O + PHOTON	$3.24 \times 10^{-12} (T/300)^{-0.66}$
R85	O ₂ ⁺ + e → O + O	$1.95 \times 10^{-7} (T/300)^{-0.7}$
R86	OH ⁺ + e → O + H	$3.75 \times 10^{-8} (T/300)^{-0.5}$
R87	H ₂ O ⁺ + e → O + H ₂	$3.9 \times 10^{-8} (T/300)^{-0.5}$
R88	H ₂ O ⁺ + e → O + H + H	$3.05 \times 10^{-7} (T/300)^{-0.5}$
R89	H ₂ O ⁺ + e → OH + H	$8.6 \times 10^{-8} (T/300)^{-0.5}$
R90	H ₃ O ⁺ + e → H ₂ O + H	$7.09 \times 10^{-8} (T/300)^{-0.5}$
R91	H ₃ O ⁺ + e → O + H ₂ + H	$5.60 \times 10^{-9} (T/300)^{-0.5}$
R92	H ₃ O ⁺ + e → OH + H ₂	$5.37 \times 10^{-8} (T/300)^{-0.5}$
R93	H ₃ O ⁺ + e → OH + H + H	$3.05 \times 10^{-7} (T/300)^{-0.5}$

Ref. McElroy et al. (2013)

- Van Grootel, V., Fernandes, C. S., Gillon, M., Jehin, E., Manfroid, J., Scudlaire, R., ... & Triaud, A. H. (2018). Stellar parameters for Trappist-1. *The Astrophysical Journal*, 853(1), 30.
- Guo, J. H. (2019). The effect of photoionization on the loss of water of the planet. *The Astrophysical Journal*, 872(1), 99.
- Haisch Jr, K. E., Lada, E. A., & Lada, C. J. (2001). Disk frequencies and lifetimes in young clusters. *The Astrophysical Journal*, 553(2), L153.
- Hamano, K., Abe, Y., & Genda, H. (2013). Emergence of two types of terrestrial planet on solidification of magma ocean. *Nature*, 497(7451), 607-610.
- Holland, H. (1984). *The chemical evolution of the atmosphere and oceans*. Princeton, NJ, Princeton University Press, 1984. 592 p.
- Hollenbach, D., & McKee, C. F. (1979). Molecule formation and infrared emission in fast interstellar shocks. I Physical processes. *The Astrophysical Journal Supplement Series*, 41, 555-592.
- Huebner, W. F., & Mukherjee, J. (2015). Photoionization and photodissociation rates in solar and blackbody radiation fields. *Planetary and Space Science*, 106, 11-45.
- Hunten, D. M. (1973). The escape of light gases from planetary atmospheres. *Journal of Atmospheric Sciences*, 30(8), 1481-1494.
- Hunten, D. M., & Strobel, D. F. (1974). Production and escape of terrestrial hydrogen. *Journal of Atmospheric Sciences*, 31(2), 305-317.
- Hunten, D. M., Pepin, R. O., & Walker, J. C. (1987). Mass fractionation in hydrodynamic escape. *Icarus*, 69(3), 532-549.
- Ikoma, M., & Genda, H. (2006). Constraints on the mass of a habitable planet with water of nebular origin. *The Astrophysical Journal*, 648(1), 696.
- Johnstone, C. P. (2020). Hydrodynamic escape of water vapor atmospheres near very active stars. *The Astrophysical Journal*, 890(1), 79.
- Kasting, J. F., & Pollack, J. B. (1983). Loss of water from Venus. I. Hydrodynamic escape of hydrogen. *Icarus*, 53(3), 479-508.
- Kasting, J. F., Whitmire, D. P., & Reynolds, R. T. (1993). Habitable zones around main sequence stars. *Icarus*, 101(1), 108-128.
- Kimura, T., & Ikoma, M. (2020). Formation of aqua planets with water of nebular origin: Effects of water enrichment on the structure and mass of captured atmospheres of terrestrial planets. *Monthly Notices of the Royal Astronomical Society*, 496(3), 3755-3766.
- Kopparapu, R. K., Ramirez, R., Kasting, J. F., Eymet, V., Robinson, T. D., Mahadevan, S., ... & Deshpande, R. (2013). Habitable zones around main-sequence stars: new estimates. *The Astrophysical Journal*, 765(2), 131.
- Kuramoto, K., & Matsui, T. (1996). Partitioning of H and C between the mantle and core during the core formation in the Earth: Its implications for the atmospheric evolution and redox state of early mantle. *Journal of Geophysical Research: Planets*, 101(E6), 14909-14932.
- Kuramoto, K., Umemoto, T., & Ishiwatari, M. (2013). Effective hydrodynamic hydrogen escape from an early Earth atmosphere inferred from high-accuracy numerical simulation. *Earth and Planetary Science Letters*, 375, 312-318.
- Lebrun, T., Massol, H., Chassefiere, E., Davaille, A., Marcq, E., Sarda, P., ... & Brandeis, G. (2013). Thermal evolution of an early magma ocean in interaction with the atmosphere. *Journal of Geophysical Research: Planets*, 118(6), 1155-1176.
- Le Teuff, Y. H., Millar, T. J., & Markwick, A. J. (2000). The UMIST database for astrochemistry 1999. *Astronomy and Astrophysics Supplement Series*, 146(1), 157-168.
- Lenzuni, P., Chernoff, D. F., & Salpeter, E. E. (1991). Rosseland and Planck mean opacities of a zero-metallicity gas. *The Astrophysical Journal Supplement Series*, 76, 759-801.
- Luger, R., & Barnes, R. (2015). Extreme water loss and abiotic O₂ buildup on planets throughout the habitable zones of M dwarfs. *Astrobiology*, 15(2), 119-143.
- Luger, R., Barnes, R., Lopez, E., Fortney, J., Jackson, B., & Meadows, V. (2015). Habitable evaporated cores: transforming mini-Neptunes into super-Earths in the habitable zones of M dwarfs. *Astrobiology*, 15(1), 57-88.
- Marty, B. (2012). The origins and concentrations of water, carbon, nitrogen and noble gases on Earth. *Earth and Planetary Science Letters*, 313, 56-66.
- McElroy, D., Walsh, C., Markwick, A. J., Cordiner, M. A., Smith, K., & Millar, T. J. (2013). The UMIST database for astrochemistry 2012. *Astronomy & Astrophysics*, 550, A36.
- Munoz, A. G. (2007). Physical and chemical aeronomy of HD 209458b. *Planetary and Space Science*, 55(10), 1426-1455.
- Murray-Clay, R. A., Chiang, E. I., & Murray, N. (2009). Atmospheric escape from hot Jupiters. *The Astrophysical Journal*, 693(1), 23.
- Hori, Y., & Ogihara, M. (2020). Do the TRAPPIST-1 planets have hydrogen-rich atmospheres?. *The Astrophysical Journal*, 889(2), 77.
- Hunten, D. M., Pepin, R. O., & Walker, J. C. (1987). Mass fractionation in hydrodynamic escape. *Icarus*, 69(3), 532-549.
- Owen, J. E., & Mohanty, S. (2016). Habitability of terrestrial-mass planets in the HZ of M Dwarfs-I. H/He-dominated atmospheres. *Monthly Notices of the Royal Astronomical Society*, 459(4), 4088-4108.
- Peacock, S., Barman, T., Shkolnik, E. L., Hauschildt, P. H., & Baron, E. (2019). Predicting the extreme ultraviolet radiation environment of exoplanets around low-mass stars: the TRAPPIST-1 system. *The Astrophysical Journal*, 871(2), 235.

- Ramirez, R. M., & Kaltenegger, L. (2014). The habitable zones of pre-main-sequence stars. *The Astrophysical Journal Letters*, 797(2), L25.
- Rothman, L. S., Gordon, I. E., Babikov, Y., Barbe, A., Benner, D. C., Bernath, P. F., ... & Wagner, G. (2013). The HITRAN2012 molecular spectroscopic database. *Journal of Quantitative Spectroscopy and Radiative Transfer*, 130, 4-50.
- Schlesinger, G., & Miller, S. L. (1983). Prebiotic synthesis in atmospheres containing CH₄, CO, and CO₂. *Journal of molecular evolution*, 19(5), 383-390.
- Tennyson, J., Yurchenko, S. N., Al-Refaie, A. F., Barton, E. J., Chubb, K. L., Coles, P. A., ... & Zak, E. (2016). The ExoMol database: molecular line lists for exoplanet and other hot atmospheres. *Journal of Molecular Spectroscopy*, 327, 73-94.
- Tian, F., Toon, O. B., Pavlov, A. A., & De Sterck, H. (2005). Transonic hydrodynamic escape of hydrogen from extrasolar planetary atmospheres. *The Astrophysical Journal*, 621(2), 1049.
- Tian, F. (2015). History of water loss and atmospheric O₂ buildup on rocky exoplanets near M dwarfs. *Earth and Planetary Science Letters*, 432, 126-132.
- Tian, F., & Ida, S. (2015). Water contents of Earth-mass planets around M dwarfs. *Nature Geoscience*, 8(3), 177-180.
- Wheatley, P. J., Loudon, T., Bourrier, V., Ehrenreich, D., & Gillon, M. (2017). Strong XUV irradiation of the Earth-sized exoplanets orbiting the ultracool dwarf TRAPPIST-1. *Monthly Notices of the Royal Astronomical Society: Letters*, 465(1), L74-L78.
- Yabe, T., Aoki, T., Sakaguchi, G., Wang, P. Y., & Ishikawa, T. (1991). The compact CIP (Cubic-Interpolated Pseudo-particle) method as a general hyperbolic solver. *Computers & Fluids*, 19(3-4), 421-431.
- Yoshida, T., & Kuramoto, K. (2020). Sluggish hydrodynamic escape of early Martian atmosphere with reduced chemical compositions. *Icarus*, 345, 113740.
- Yoshida, T., & Kuramoto, K. (2021). Hydrodynamic escape of an impact-generated reduced proto-atmosphere on Earth. *Monthly Notices of the Royal Astronomical Society*, 505(2), 2941-2953.
- Yurchenko, S. N., Tennyson, J., Miller, S., Melnikov, V. V., O'Donoghue, J., & Moore, L. (2020). ExoMol line lists-XL. Rovibrational molecular line list for the hydronium ion (H₃O⁺). *Monthly Notices of the Royal Astronomical Society*, 497(2), 2340-2351.
- Zahnle, K., Kasting, J. F., & Pollack, J. B. (1990). Mass fractionation of noble gases in diffusion-limited hydrodynamic hydrogen escape. *Icarus*, 84(2), 502-527.